Schweizerischer Erdbebendienst
Service Sismologique Suisse
Servizio Sismico Svizzero
Swiss Seismological Service

ETH zürich

SITE CHARACTERIZATION REPORT

SDES: Delémont (JU) - Hôpital du Jura

Manuel Hobiger, Donat Fäh

Last Modification: 26/02/2020

Schweizerischer Erdbebendienst (SED)
Service Sismologique Suisse
Servizio Sismico Svizzero
Servizi da Terratrembels Svizzer

ETH Zürich
Sonneggstrasse 5
8092 Zürich
Schweiz
manuel.hobiger@sed.ethz.ch

Contents

Summary

The free-field strong-motion station SDES was built next to the Hôpital du Jura in Delémont (JU). We performed a passive seismic array measurement with two array configurations to characterize the soil underneath the station.
The measurements show that the fundamental frequency of the structure beneath the station is about 1.79 Hz (determined by RayDec) and corresponds to a singularity in ellipticity. The array measurements were analyzed with different techniques, namely 3-component HRFK, WaveDec and SPAC. The dispersion curves for Love and Rayleigh waves measured with both arrays do not fit together, therefore the results of the smaller array measurement were not used further. For the larger array, the dispersion curves were measured from 1.76 to 4.92 Hz for Love waves and from 2.48 to 5.11 Hz for Rayleigh waves.
The joint inversion of the Love wave dispersion curve with the Rayleigh wave dispersion and ellipticity curves showed that the structure can be explained by models with S-wave velocities of around 480 m/s down to about 65 m of depth, where the velocity increases to over 1400 m/s. At the surface, there might be a layer with low velocities of around 150 m/s with a thickness of less than 1.5 m. The V_{S30} of the best models is about 457 m/s, corresponding to soil class B in EC8 and C in SIA261.

1 Introduction

In the framework of the second phase of the Swiss Strong Motion Network (SSMNet) renewal project, a new station was planned in Delémont (JU).
The site selection resulted in the Hôpital du Jura as the best site in the area. The new station, called SDES, went operational on 4 February 2016. The location of the station is shown in Fig. 1.

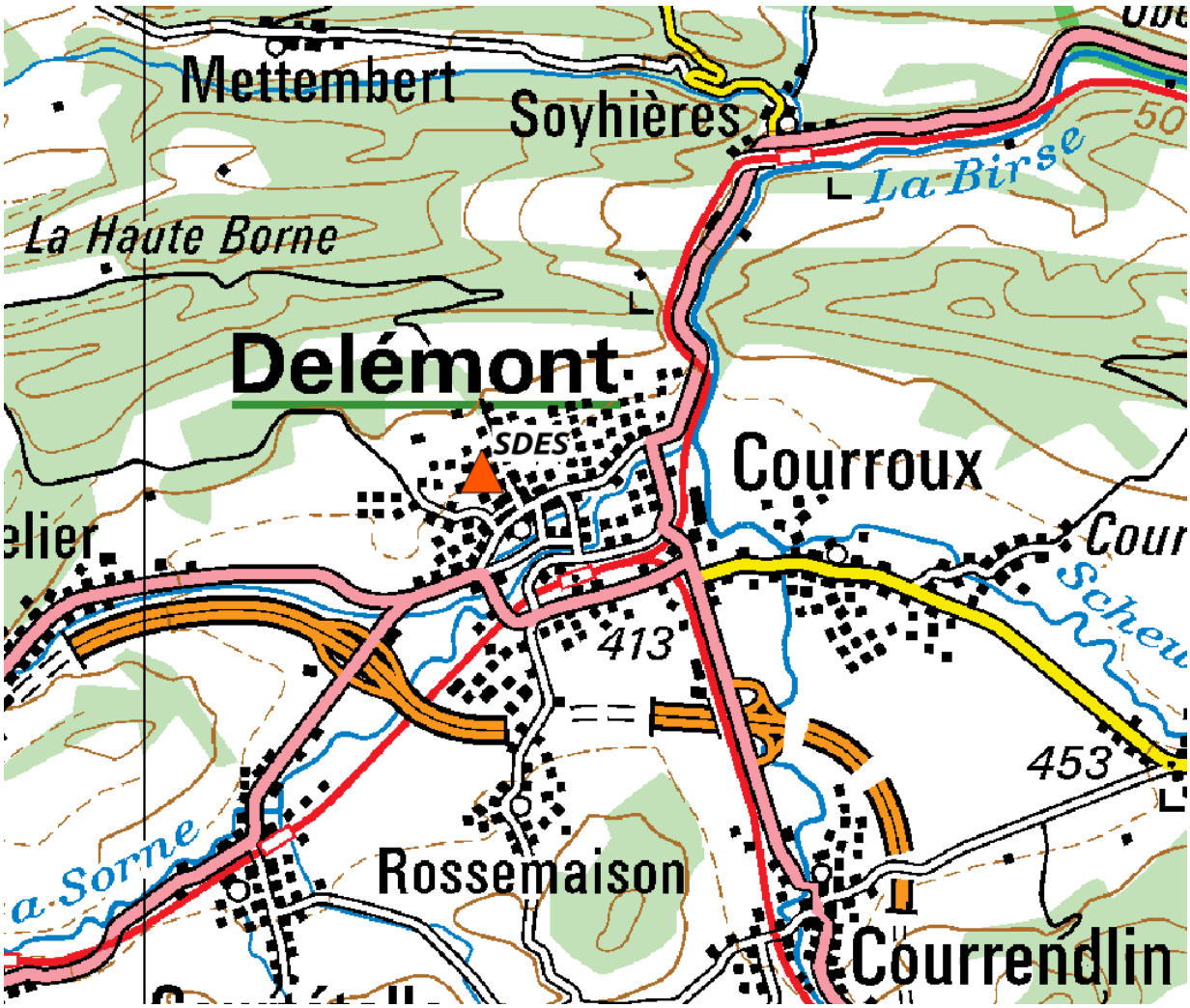

Figure 1: Map showing the location of station SDES in Delémont.

2 Geological setting

A geological map of the surroundings of station SDES is shown in Fig. 2. The geology around the station is rather complex. According to the map, the station itself and the hospital building are located on fine-grained scree. To the south, argillaceous weathering deposits are found, and micrite to the north.

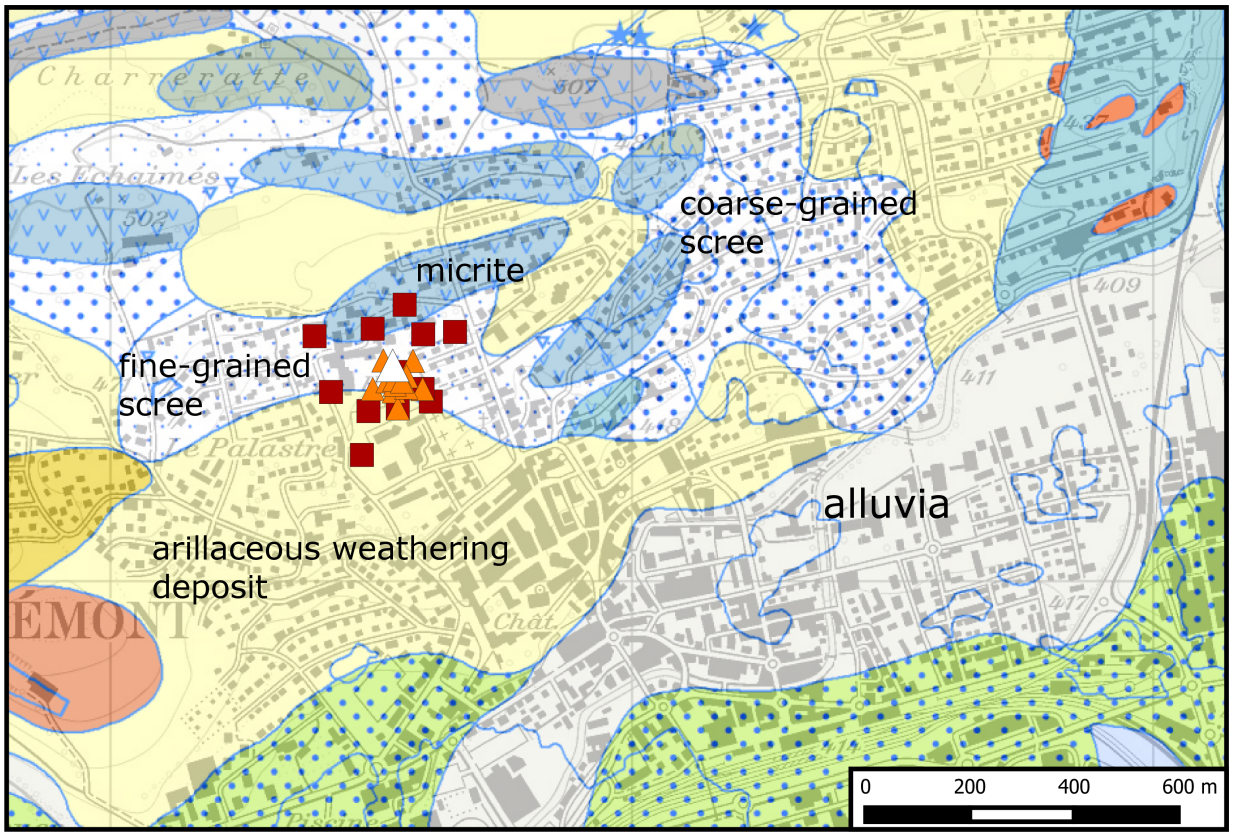

Figure 2: Geological map of the area around station SDES. The white triangle shows the location of station SDES, the orange triangles and red squares the stations of arrays 1 and 2, respectively (see Fig. 3).

3 Site characterization measurements

3.1 Data set

In order to characterize the local underground structure around station SDES, passive seismic array measurements were carried out on 4 May 2016. The layout of the seismic measurements is shown in Fig. 3.
Two array measurements were performed (see Table 1 for the main characteristics). The first array consisted of 16 stations. It was planned to consist of three rings of five stations each around a central station. The permanent station SDES was lying inside this array. The ring radii were planned to be 8 m, 20 m and 50 m, respectively. The final minimum and maximum inter-station distances in the first array were 7.7 m and 96.0 m. The names of the stations of the first array are composed of "SDES" followed by a two-digit number (42 to 49, 52 to 55, 63, 65, 68 and 74). The seismic stations consisted of Lennartz 3C 5 s sensors connected to Centaur digitizers. A total of 12 digitizers were used, with twelve sensors (those with numbers below 60) connected to the A channels and four sensors (with numbers above 60) to B channels of the digitizers.
The second array consisted of 12 stations. For this array, the station layout was not regular. The minimum and maximum inter-station distances of the second array were 28.8 and 299.3 m. All twelve sensors were connected to the A channels of the respective digitizers. The station names are composed of "SDES" and a two-digit number between 82 and 95 (82-89 and 92-95). The sensor closest to SDES (SDES44 in array 1 and SDES84 in array 2) and two other stations of the first array were kept for the second array.
The station locations have been measured by a differential GPS system (Leica Viva GS10) which was set up to measure with a precision better than 5 cm. This precision was achieved for all stations except three. For SDES47, the precision was 9.3 cm. For SDES87, it was 5.7 cm, and for SDES95, it was 13.5 cm.

Table 1: List of the passive seismic array measurements in Delémont.

Array name	Number of sensors	Minimum interstation distance [m]	Maximum interstation distance [m]	Recording time [s]
1	16	7.7	96.0	7500
2	12	28.8	299.3	7200

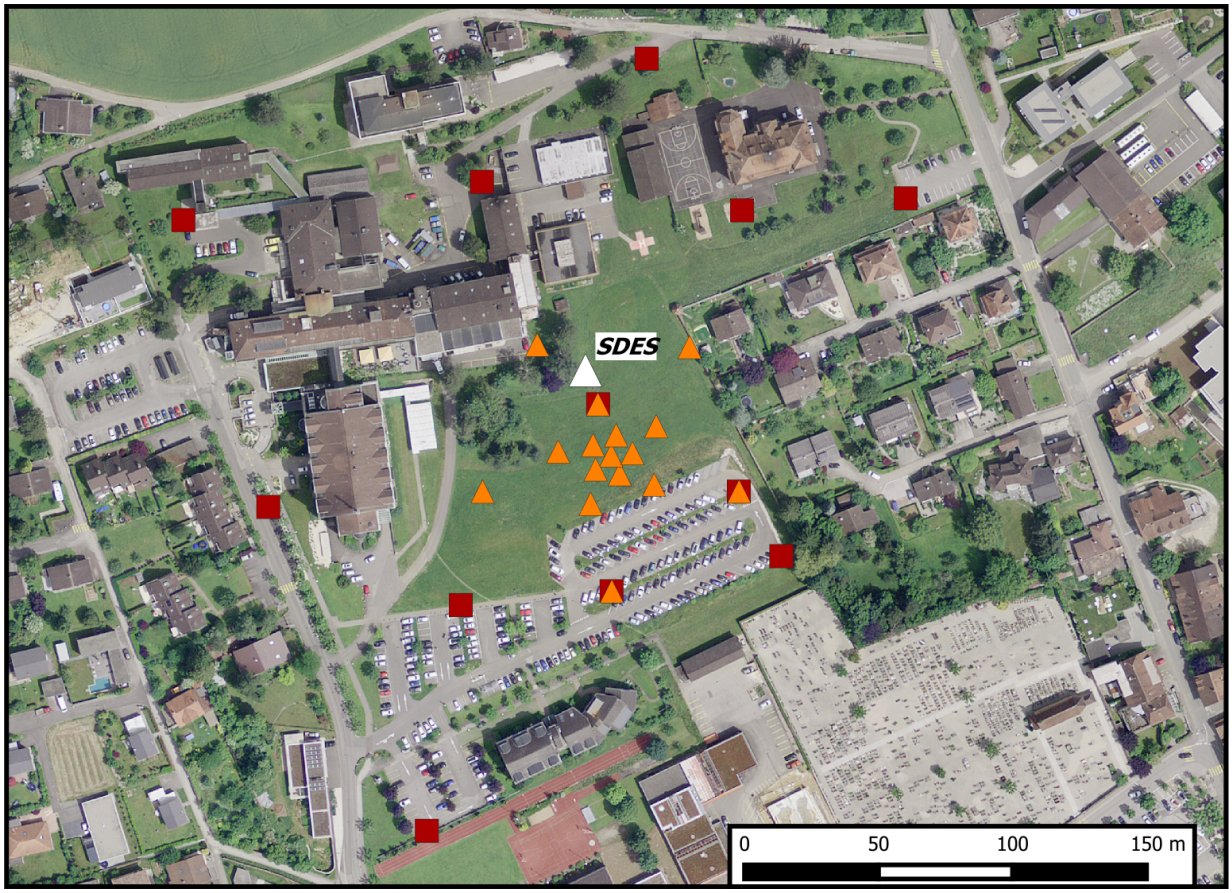

Figure 3: Layout of the array measurements around station SDES. The location of SDES is indicated by the white triangle, the locations of the stations for the passive seismic measurement by the orange triangles (first array) and red squares (second array). ©2019 swisstopo (JD100042)

3.2 H/V and RayDec ellipticity curves

Figure 4 shows the H/V curves determined with the time-frequency analysis method (Fäh et al., 2009) for all stations of both passive arrays. For all curves, we can clearly identify the peak frequency between 1.27 and 1.75 Hz, followed by a strong decrease and a trough at around 3 Hz.
The RayDec technique (Hobiger et al., 2009) is supposed to eliminate the contributions of other wave types than Rayleigh waves and give a better estimate of the ellipticity than the classical H/V technique. The RayDec ellipticity curves for all stations of the array measurements are shown in Fig. 4. Station SDES44, the station closest to SDES, serves as a reference and will be used for the inversion. This station has a peak frequency of 1.65 Hz (H/V) or 1.79 Hz (RayDec).
In both the H/V and RayDec curves, we can distinguish two classes of curves. The ones with higher amplitude and slightly higher peak frequency belong to stations of the small array. For the stations of the large array, the curves show more variation, but are mostly still in good agreement.

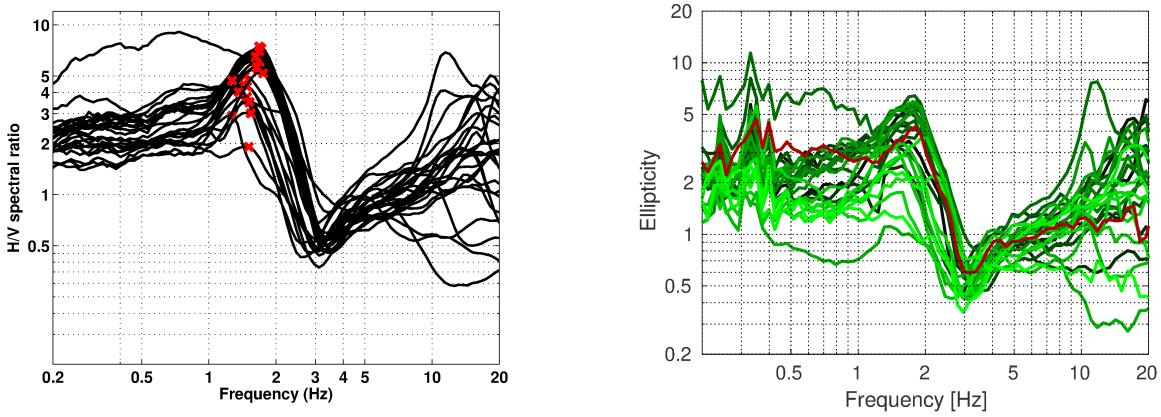

Figure 4: Left: Overview of the H/V measurements for the different stations of both array measurements. Right: RayDec ellipticities for all measurement stations. The red curve corresponds to SDES44, the station closest to SDES in array 1.

3.3 Polarization measurements

The polarization analysis was performed according to Burjánek et al. (2010) and Burjánek et al. (2012). The results for all stations of the array are similar. Only the results for SDES44 are shown here.
We see a slight predominance of strikes along 45°-135°, but no preferential linear particle polarization and we do not interpret this as indication for 2-dimensional polarization effects.

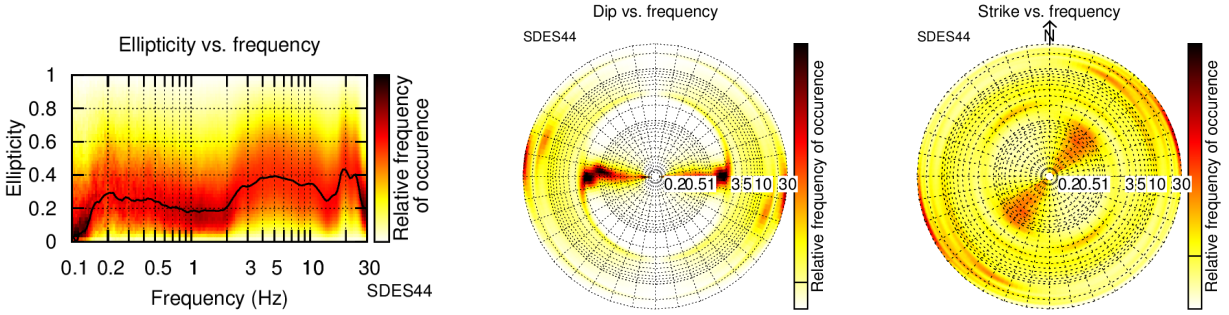

Figure 5: Polarization analysis of station SDES44.

3.4 3-component high-resolution FK

The results of the 3-component high-resolution FK analysis (Poggi and Fäh, 2010) are shown in Fig. 6 (dispersion curves) and Fig. 7 (ellipticity curves). On the transverse component, corresponding to Love waves, we can clearly identify a dispersion curve for array 1 between 5.5 and 15.1 Hz and for array 2 between 1.7 and 4.9 Hz. The curve for array 1 is relatively flat and does not reach the upper-frequency resolution limit at all. The curve for array 2 follows a clear dispersive trend of decreasing velocities with frequency, but it is not retrieved above 5 Hz, even if the theoretical array resolution limit would be higher.
On the vertical component, corresponding to Rayleigh waves, we see a dispersion curve with increasing velocity from 4.2 to 23.4 Hz for array 1. For array 2, we see a decreasing dispersive mode between 2.4 and 5.3 Hz. On the radial component, also related with Rayleigh waves, the curve for array 1 looks very similar to the curve of the transverse component, indicating a possible leaking of the Love waves on the radial component. For array 2, the result on the radial component is similar to the vertical component, but less clear and no curve was picked.
The corresponding ellipticity curves of these modes (Fig. 7) are mostly flat for array 1. For array 2, we can identify a trough at around 3 Hz.

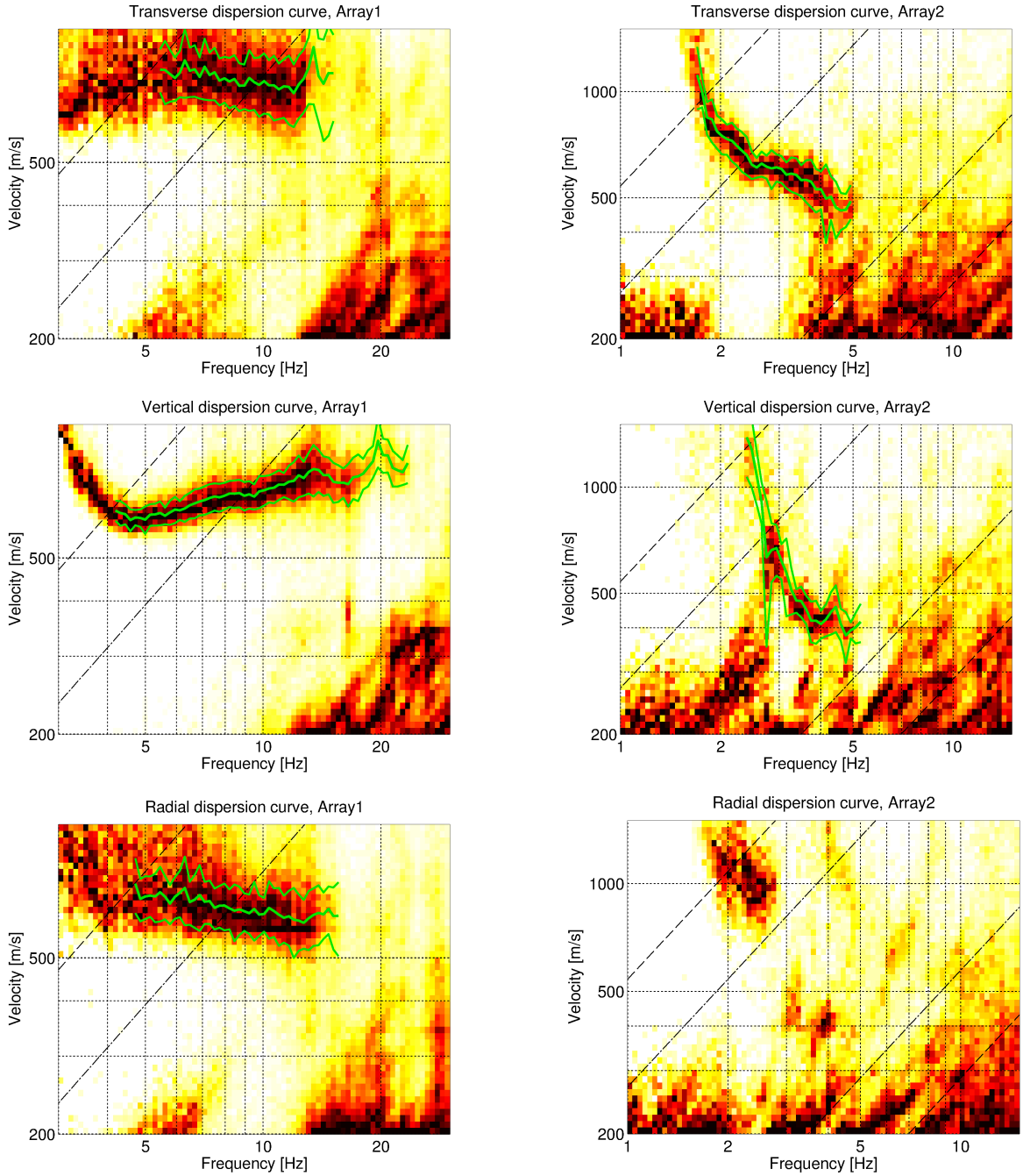

Figure 6: Dispersion curves obtained with the 3-component HRFK algorithm (Poggi and Fäh, 2010). In the left column, the dispersion curves for the transverse, vertical and radial components are shown for array 1, and in the right column for array 2. The dashed and dotted black lines are the array resolution limits. The solid green lines are picked from the data, where the central line indicates the best values and the two outer lines the standard deviation.

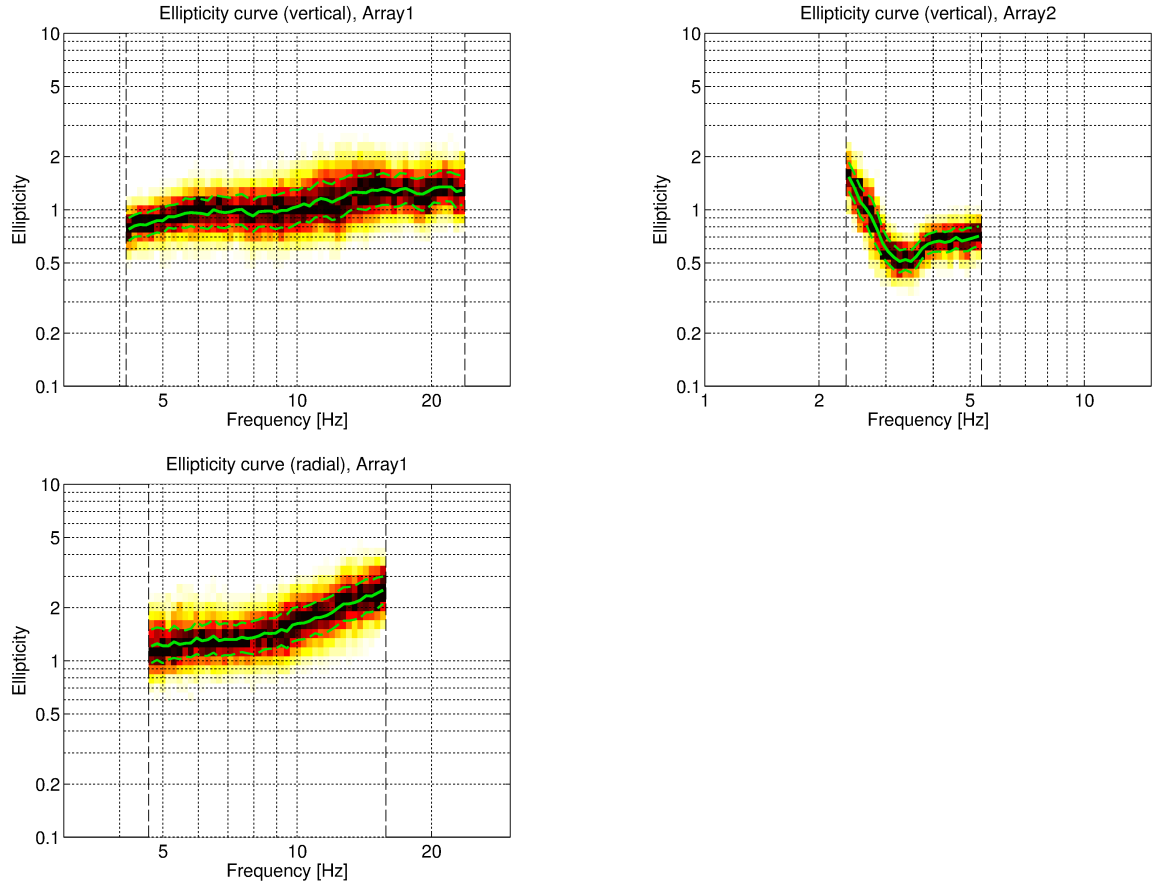

Figure 7: Ellipticity curves obtained with the 3-component HRFK algorithm (Poggi and Fäh, 2010) corresponding to the picked dispersion curves on the vertical and radial components for array 1 (left column) and array 2 (right column). The solid green lines are picked from the data, where the central line indicates the best values and the two outer lines the standard deviation.

3.5 WaveDec

The results of the WaveDec (Maranò et al., 2012) processing are shown in Figs 8 and 9. This technique estimates the properties of single or multiple waves simultaneously with a maximum likelihood approach. In order to get good results, the parameter γ, which modifies the sharpness of the wave property estimation, has been tuned. Here, a value of $\gamma = 0.2$ was used, corresponding to a mainly maximum likelihood estimation.
For array 1, no Love wave dispersion curve could be identified. For array 2, we can retrieve the dispersion curve between 1.6 and 3.1 Hz, not reaching the higher-frequency resolution limit of the array.
For Rayleigh waves, we see a dispersion curve with increasing velocities between 3.9 and 14.5 Hz for array 1. For array 2, we can identify a dispersion curve between 2.0 and 5.1 Hz, but the picking is not very clear. The ellipticity angle for the picked Rayleigh wave dispersion curve of array 1 is always negative, indicating retrograde particle motion. For array 2, it is positive below around 3 Hz and negative above, indicating a change from prograde to retrograde particle motion here.

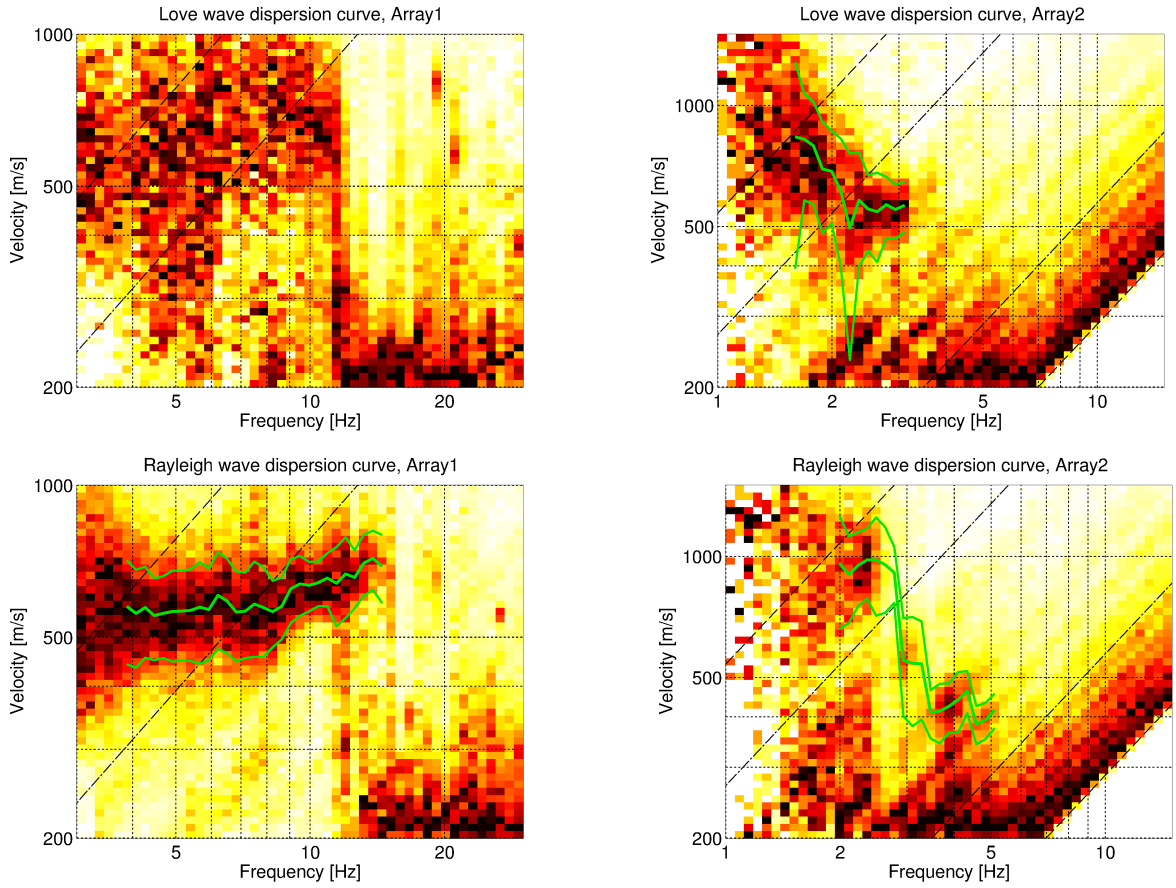

Figure 8: Love (top line) and Rayleigh (bottom line) wave dispersion curves obtained with the WaveDec technique (Maranò et al., 2012) for array 1 (left) and array 2 (right). The dashed lines indicate the theoretical array resolution limits.

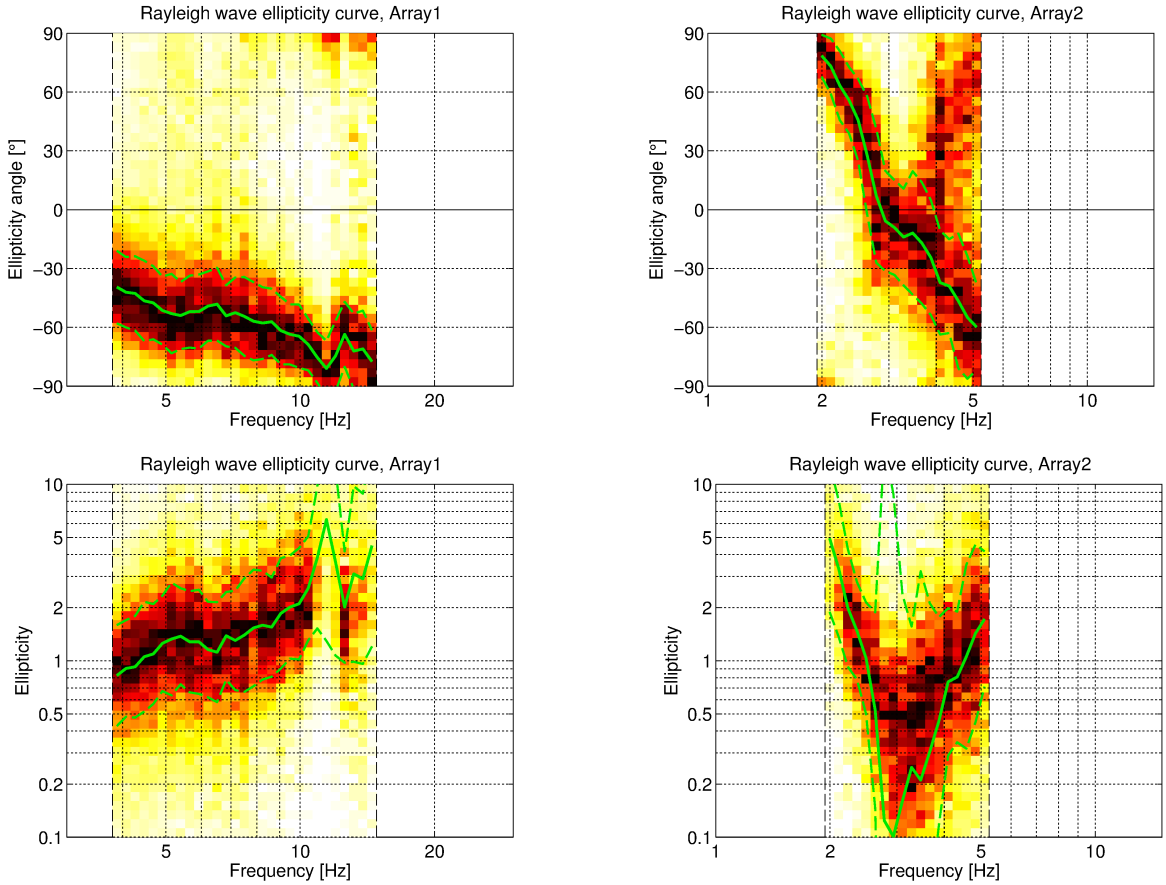

Figure 9: Rayleigh wave ellipticity curves obtained with the WaveDec technique (Maranò et al., 2012). Top line: Rayleigh wave ellipticity angles obtained using array 1 (left) and array 2 (right). Bottom line: Rayleigh wave ellipticity curve, i.e. the absolute value of the tangent of the ellipticity angle, for the curve of array 1 (left) and array 2 (right).

3.6 SPAC

The SPAC (Aki, 1957) curves of the vertical components have been calculated using the M-SPAC (Bettig et al., 2001) technique implemented in geopsy. Rings with different radius ranges had been defined previously and for all station pairs with distance inside this radius range, the cross-correlation was calculated in different frequency ranges. These cross-correlation curves are averaged for all station pairs of the respective ring and give the SPAC curves. The rings are defined in such a way that at least three station pairs contribute and that their connecting vectors have a good directional coverage.
The SPAC curves for all defined rings are shown in Fig. 10 for array 1 and Fig. 11 for array 2. The black points indicate the data values which contributed to the final dispersion curve estimation, which was made with the function `spac2disp` of the geopsy package. These resulting dispersion curves are shown in Fig. 12.
The SPAC curves for the different ring radii differ a lot from Bessel functions and can only partly be interpreted. At around 1 Hz, for example, most curves for array 1 show an uncommon trough. As a consequence, the estimated dispersion curves should be interpreted with care. We can nevertheless retrieve Rayleigh wave dispersion curves between 3.1 and 6.5 Hz for array 1 and between 2.3 and 2.9 Hz for array 2.

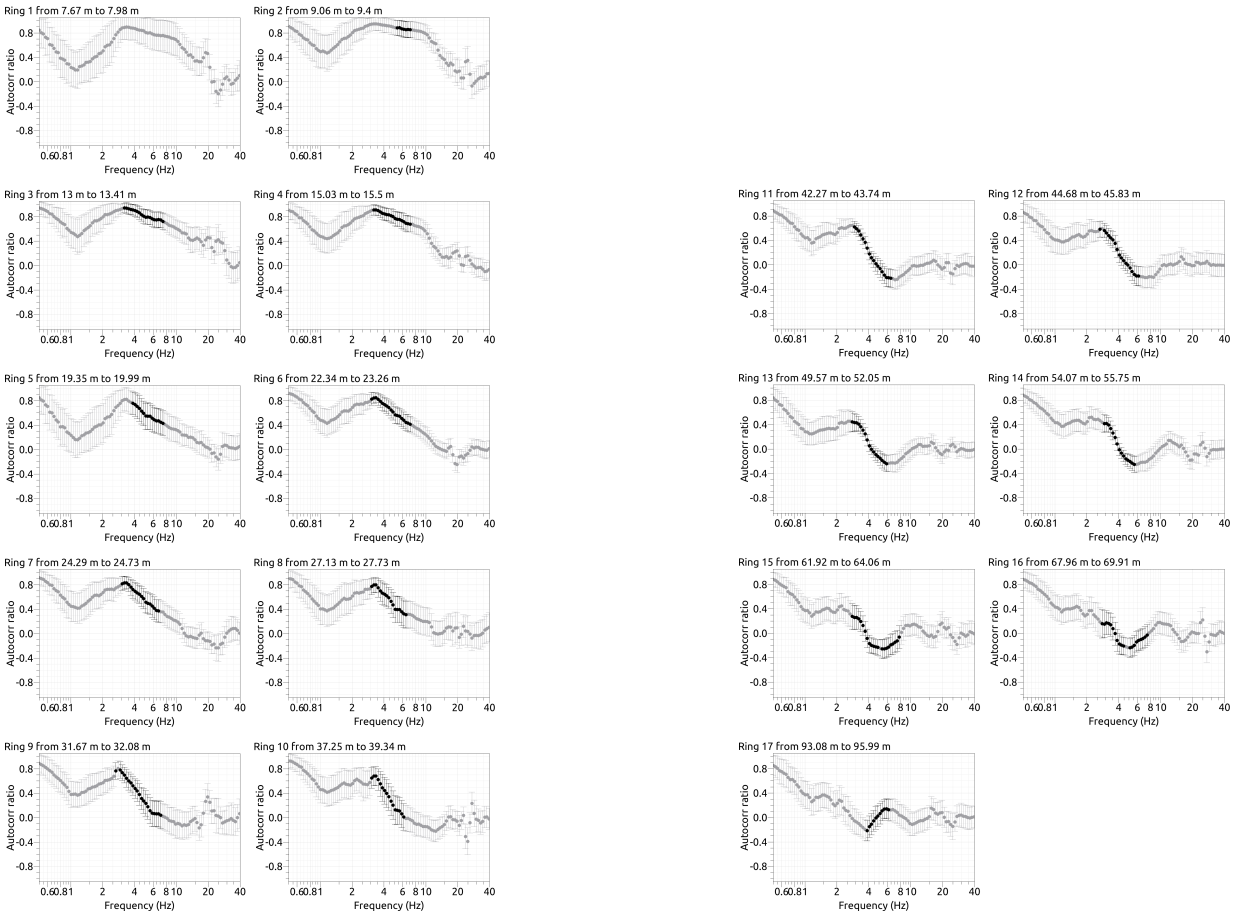

Figure 10: SPAC curves for array 1. The black data points contributed to the dispersion curve estimation.

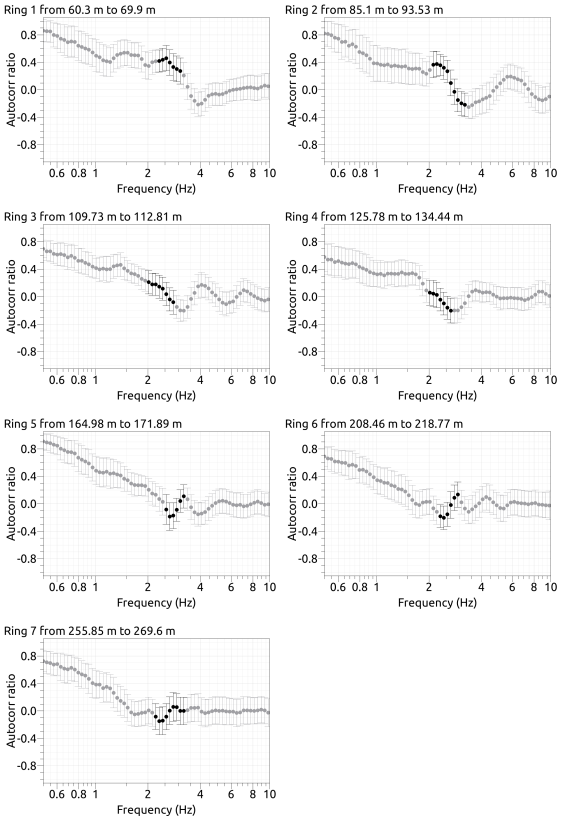

Figure 11: SPAC curves for array 2. The black data points contributed to the dispersion curve estimation.

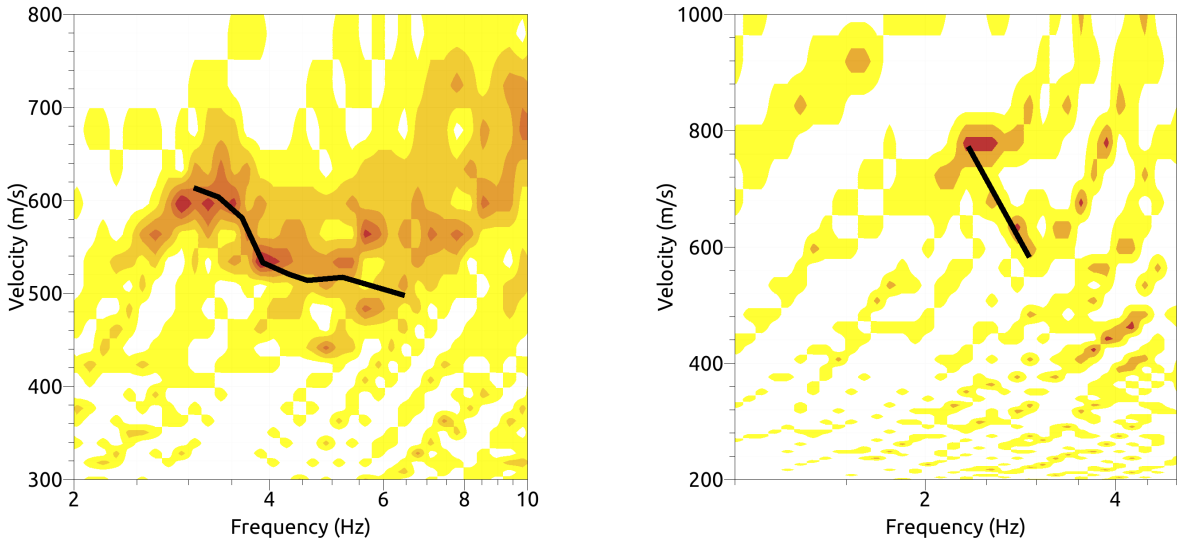

Figure 12: Resulting Rayleigh wave velocities for array 1 (left) and array 2 (right). The black line corresponds to the picked dispersion curve.

3.7 Summary

Fig. 13 gives an overview of the dispersion and ellipticity curves determined by the different methods.
For Love waves, the curves from array 1 and array 2 do not seem to fit together, at least not if both represent the fundamental mode. For array 1, the HRFK and WaveDec results show some discrepancies, but are in general agreement.
For Rayleigh waves, we also observe the incompatibility of the two arrays, at least if the fundamental mode was seen in both arrays. For array 1, HRFK and WaveDec show rather flat dispersion curves, with even a slight velocity increase with frequency. For array 2, HRFK and WaveDec are in good agreement above 2.6 Hz. Below, the WaveDec curve is less trustworthy because of the unclear picking there (Fig. 8). The SPAC curves are not fitting well with the other methods, also because they were not well determined.
The ellipticity curves retrieved using the different methods are in better qualitative agreement than the dispersion curve. Here we use the single-station ellipticity curve determined with RayDec for station SDES44, closest to SDES, as a comparison. It shows an ellipticity peak at 1.79 Hz. The array methods do not resolve these low frequencies. Above, WaveDec and HRFK show a trough at around 3 Hz, which is in good agreement with the RayDec curve. At higher frequencies, the curves obtained for array 1 are in surprisingly good agreement with the RayDec curve. In the ellipticity angle representation, all curves except WaveDec are plotted twice, corresponding to retrograde particle motion (with negative angles) and the second to prograde particle motion (with positive angles). From the WaveDec curve, we see that the particle motion changes from prograde to retrograde at 2.9 Hz. As we interpret this curve as belonging to the fundamental mode and this mode has a retrograde particle motion at low frequencies, we conclude that the ellipticity peak observed at 1.79 Hz must correspond to a singularity, where the true ellipticity value goes towards infinity and the angle is $\pm 90^\circ$.

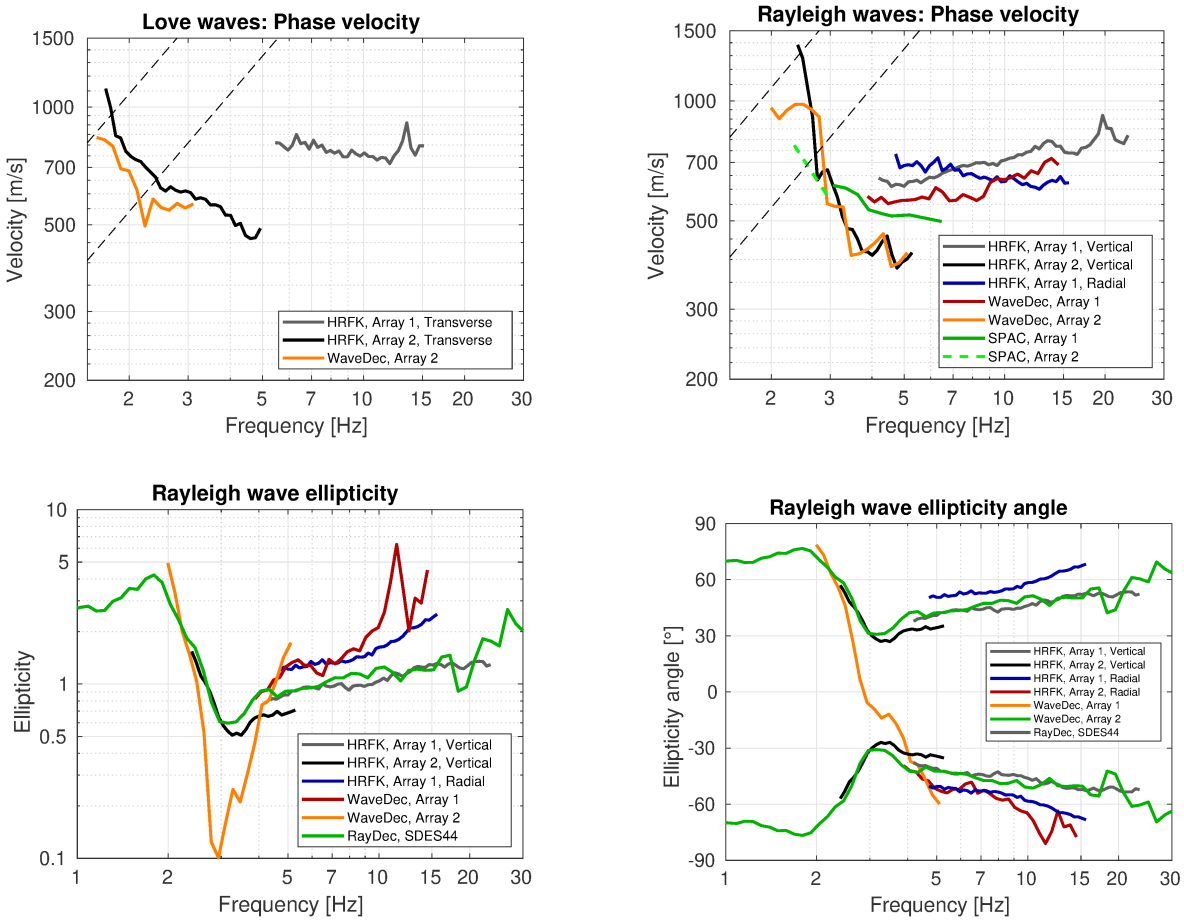

Figure 13: Overview of the Love and Rayleigh wave dispersion curves as well as the ellipticity curves for both arrays. The dashed lines indicate the theoretical resolution limits of the array. The RayDec ellipticity curve corresponds to station SDES44.

4 Data inversion

4.1 Inversion targets

The picking quality and mode attribution of the dispersion curves for array 1 is questionable. Therefore, we did not further use this data.
For the inversion of the data for the subsurface structure, we finally used the Love and Rayleigh wave dispersion curves measured using HRFK for array 2 as main targets. The ellipticity angle information was used as additional target. The WaveDec ellipticity angle for array 2 was used to this purpose and an additional part of the RayDec curve at lower frequency, in order to fix the ellipticity peak, i.e. the position where the ellipticity angle changes from $+90°$ to $-90°$. Anyhow, the target fixes the particle motion to be retrograde below 1.7 Hz and prograde above 2.05 Hz, without actually fixing the frequency of change.
The details of the inversion targets are indicated in Table 2 and the corresponding curves are shown in Fig. 14.

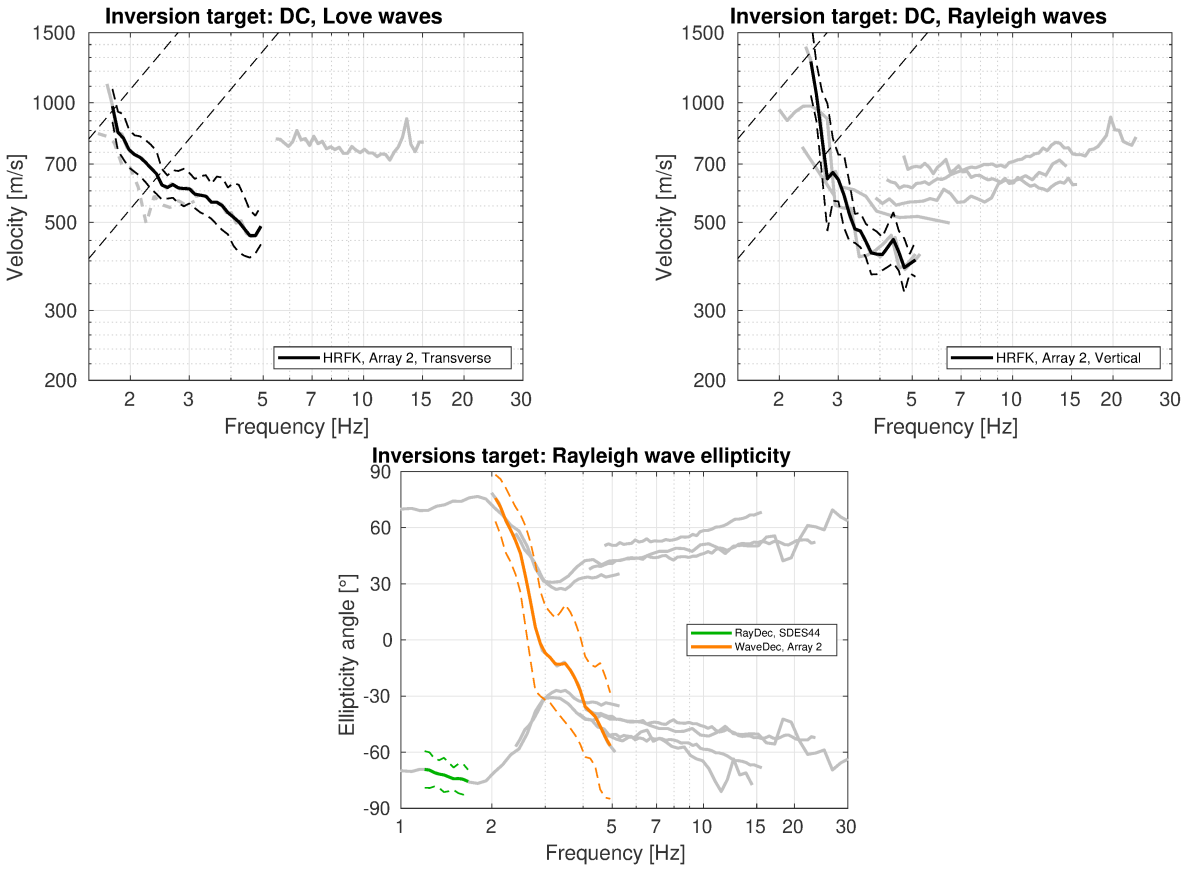

Figure 14: Overview of the dispersion (left) and ellipticity (right) curves used as targets for the different inversions.

Table 2: List of the different data curves used as target in the different inversions. The Love wave dispersion curves were not used in the final reference inversions.

Array	Method	Wave type	Mode	Curve type	Frequency range [Hz]
2	HRFK (T)	Love	fundamental	dispersion	1.76 - 4.92
2	HRFK (V)	Rayleigh	fundamental	dispersion	2.48 - 5.11
	RayDec (SDES44)	Rayleigh	fundamental	ellipticity	1.20 - 1.70
2	WaveDec	Rayleigh	fundamental	ellipticity	2.05 - 4.92

4.2 Inversion parameterization

For the inversion, six different parameterizations have been used in total. The first five had free values of the depths and velocities of the different layers, ranging from four to eight layers (including half-space). The last parameterization had fixed layer depths and consisted of 15 layers in total. The P-wave velocities were allowed to vary up to 5000 m/s. The S-wave velocities were allowed to range from 50 to 3500 m/s. The deepest layer interfaces were parameterized to occur at a maximum depth of 200 m. The density was fixed to 1 900 kg/m^3 for the topmost two layers, to 2 300 kg/m^3 for the lowest layer and to 2 100 kg/m^3 for all other layers. No low-velocity zones were allowed.

4.3 Inversion results

We performed six inversions with different parameterizations for the different targets. In Table 3, the obtained minimum misfit values are shown Each inversion run produced around 150 000 total models in order to assure a good convergence of the solution. The results of the different inversions are shown in Figs 15 - 20.
The minimum misfit values achieved in the different inversions are similar. In all inversion runs, the Love and Rayleigh wave dispersion curves are fitted in a similar way. However, the velocities of the Love waves are in general slightly under- and those of the Rayleigh waves slightly over-estimated, but both are in the range of the error bars. The best models of all inversions have ellipticity peak frequencies of 1.9 Hz, not far from the 1.79 Hz measured for SDES44.

Table 3: List of inversions

Inversion	Number of layers	Number of models	Minimum misfit
SDES4l	4	100 047	0.692
SDES5l	5	150 050	0.692
SDES6l	6	150 031	0.719
SDES7l	7	150 027	0.720
SDES8l	8	150 005	0.721
SDESfix	15	149 998	0.753

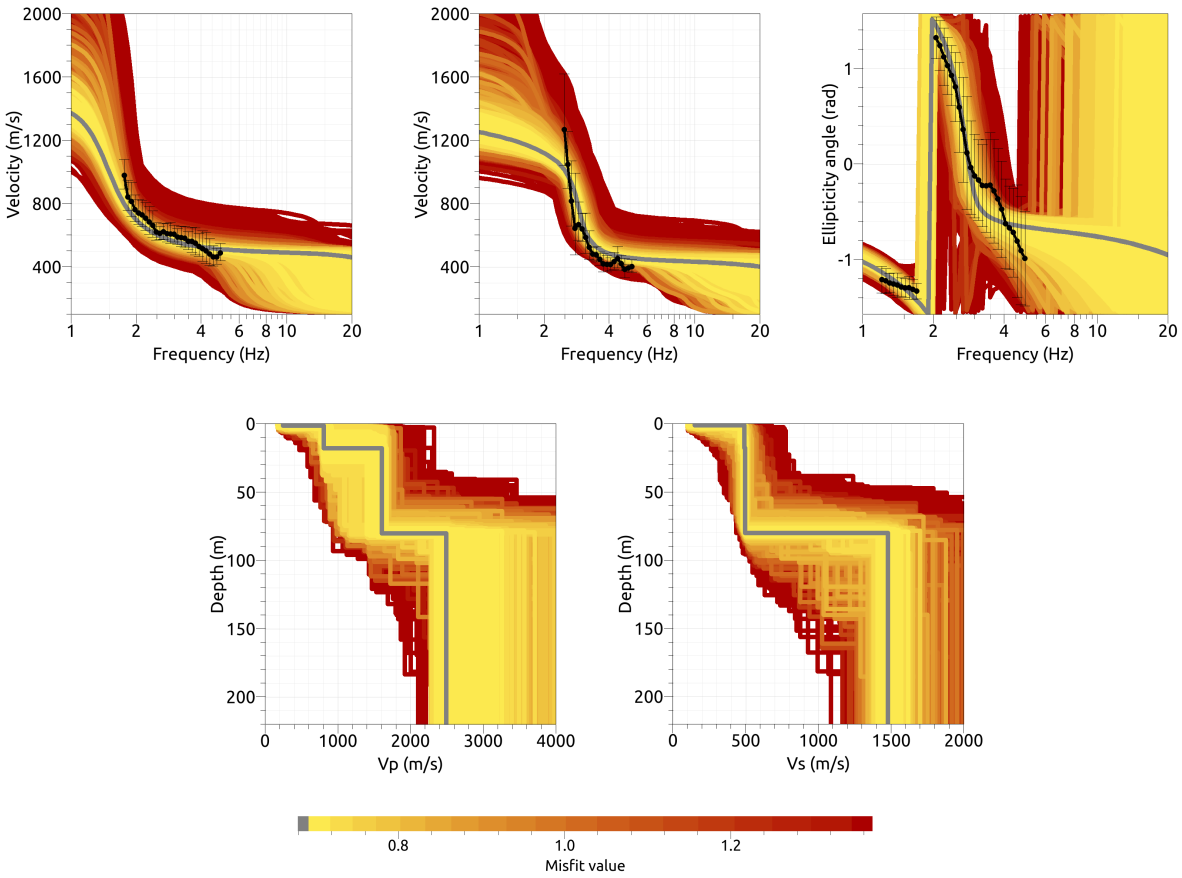

Figure 15: Inversion SDES4l. Top line: Dispersion curves for the Love wave fundamental mode (left) and the Rayleigh wave fundamental mode (center) and ellipticity curves of the Rayleigh wave fundamental mode (right). Bottom line: P-wave velocity profiles (left) and S-wave velocity profiles (right). The black dots indicate the data points used for the inversion, the gray line indicates the best-fitting model.

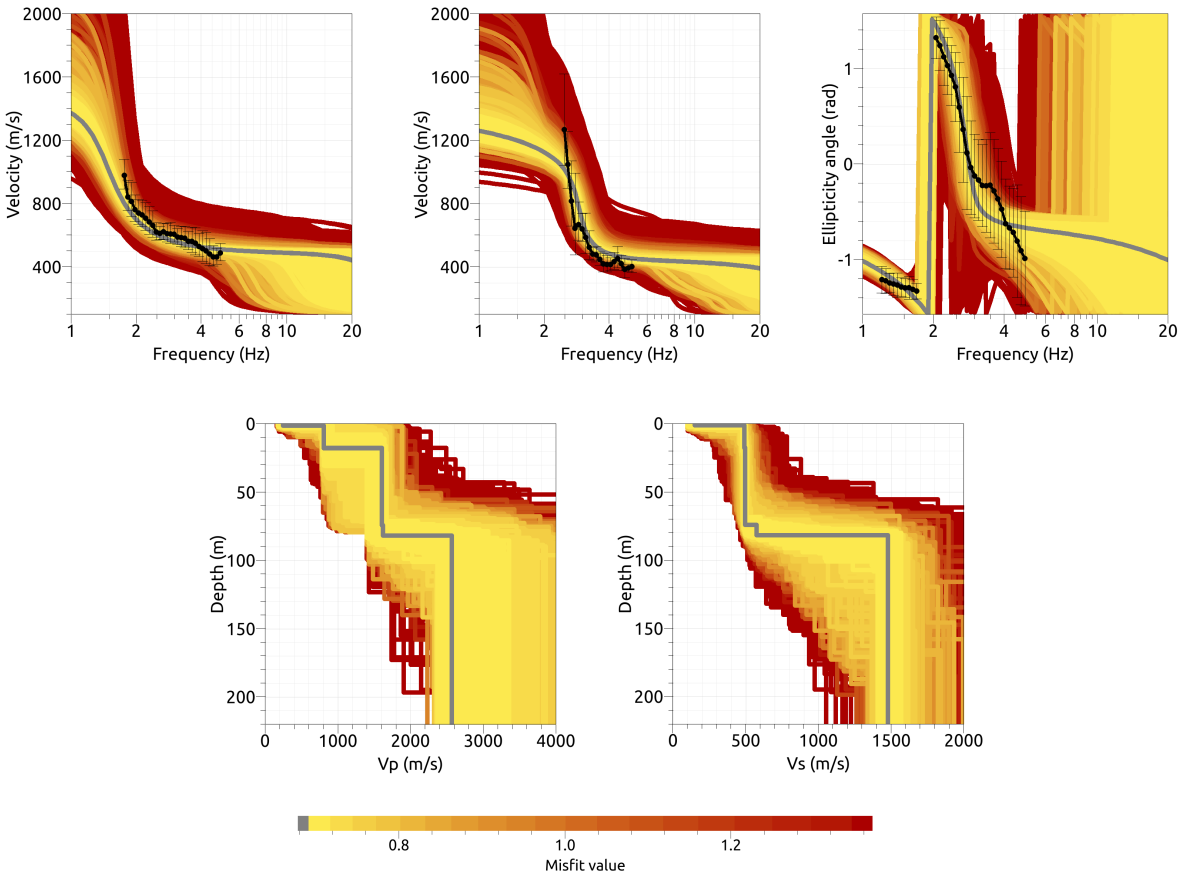

Figure 16: Inversion SDES5l. Top line: Dispersion curves for the Love wave fundamental mode (left) and the Rayleigh wave fundamental mode (center) and ellipticity curves of the Rayleigh wave fundamental mode (right). Bottom line: P-wave velocity profiles (left) and S-wave velocity profiles (right). The black dots indicate the data points used for the inversion, the gray line indicates the best-fitting model.

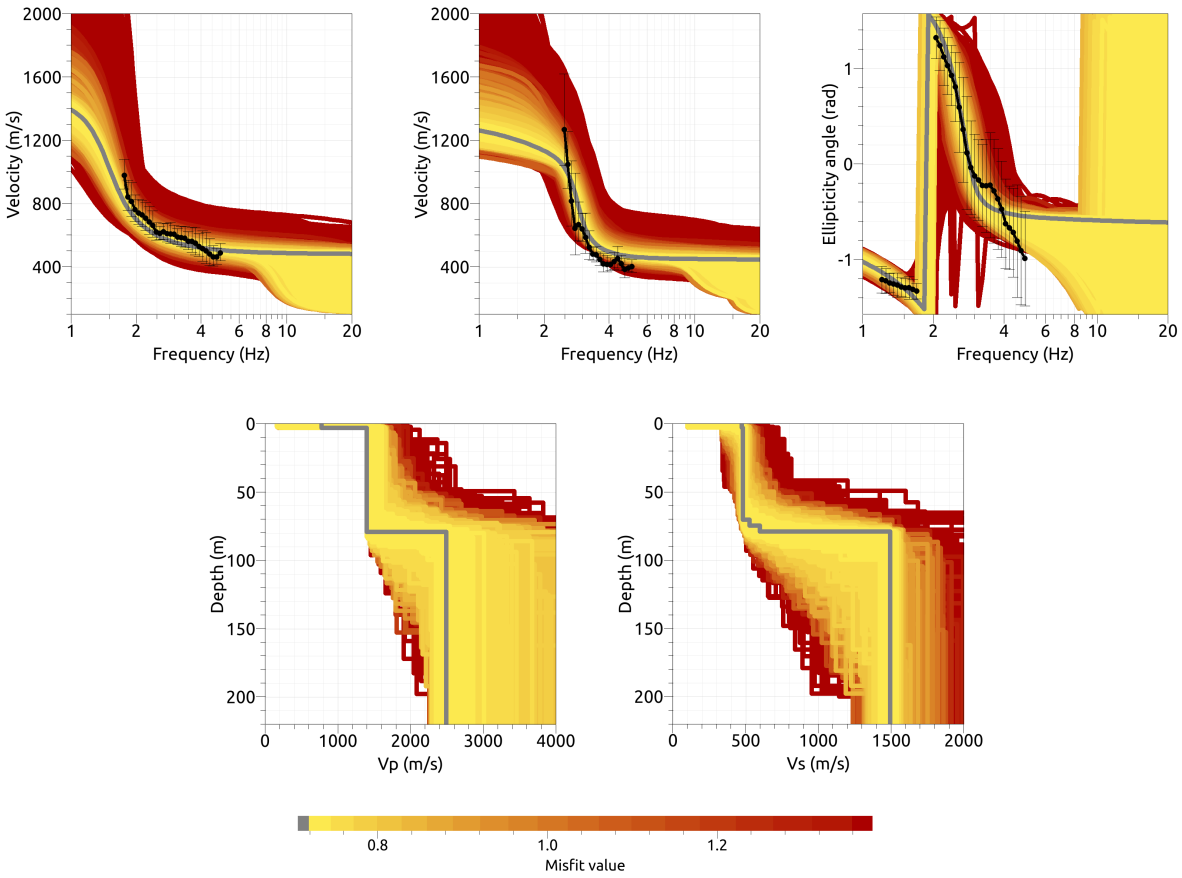

Figure 17: Inversion SDES6l. Top line: Dispersion curves for the Love wave fundamental mode (left) and the Rayleigh wave fundamental mode (center) and ellipticity curves of the Rayleigh wave fundamental mode (right). Bottom line: P-wave velocity profiles (left) and S-wave velocity profiles (right). The black dots indicate the data points used for the inversion, the gray line indicates the best-fitting model.

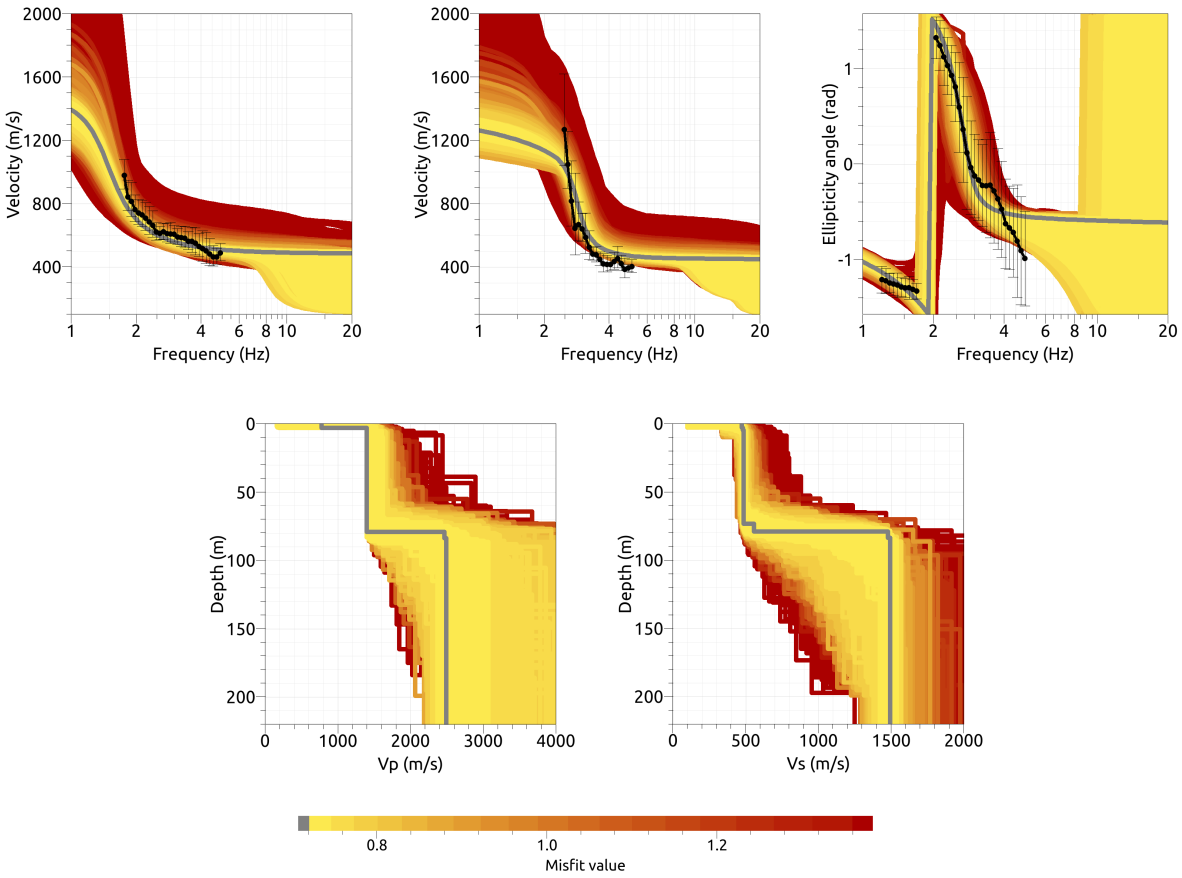

Figure 18: Inversion SDES7l. Top line: Dispersion curves for the Love wave fundamental mode (left) and the Rayleigh wave fundamental mode (center) and ellipticity curves of the Rayleigh wave fundamental mode (right). Bottom line: P-wave velocity profiles (left) and S-wave velocity profiles (right). The black dots indicate the data points used for the inversion, the gray line indicates the best-fitting model.

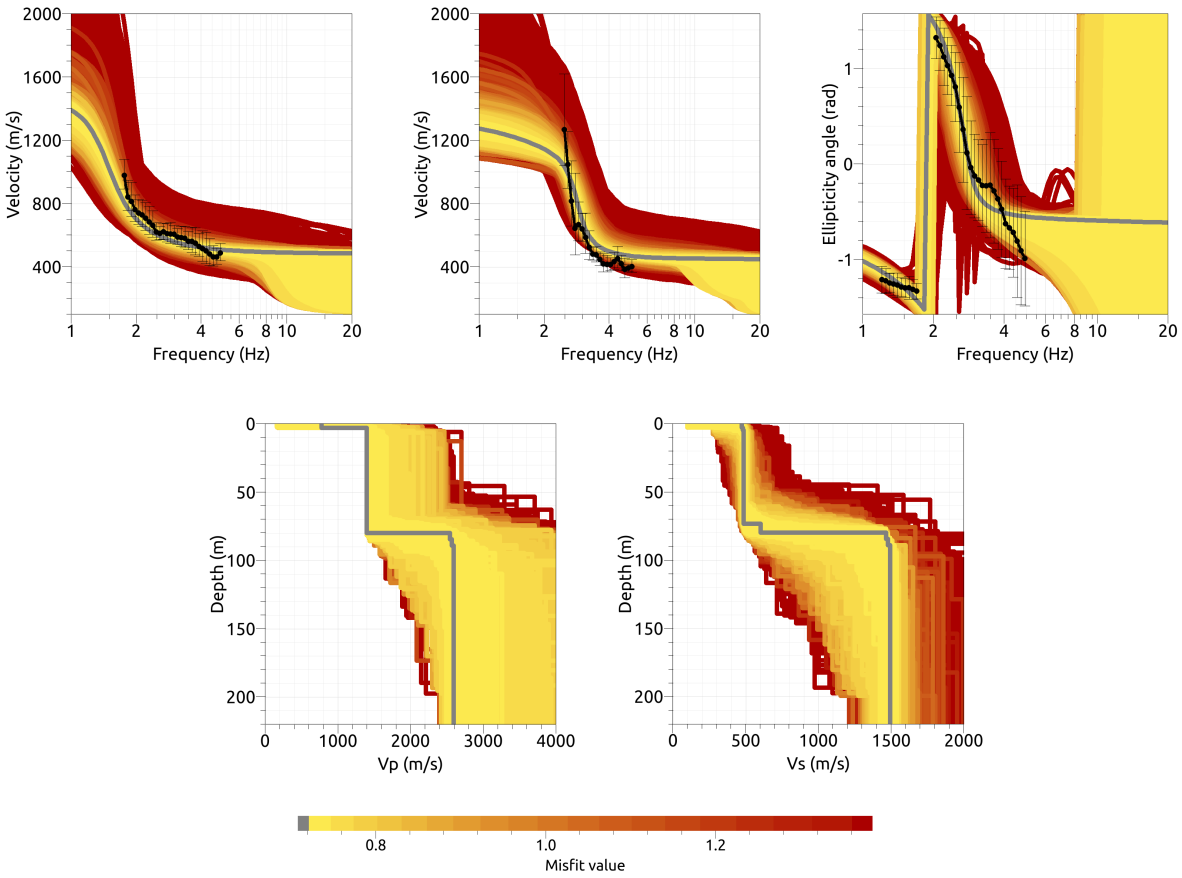

Figure 19: Inversion SDES8l. Top line: Dispersion curves for the Love wave fundamental mode (left) and the Rayleigh wave fundamental mode (center) and ellipticity curves of the Rayleigh wave fundamental mode (right). Bottom line: P-wave velocity profiles (left) and S-wave velocity profiles (right). The black dots indicate the data points used for the inversion, the gray line indicates the best-fitting model.

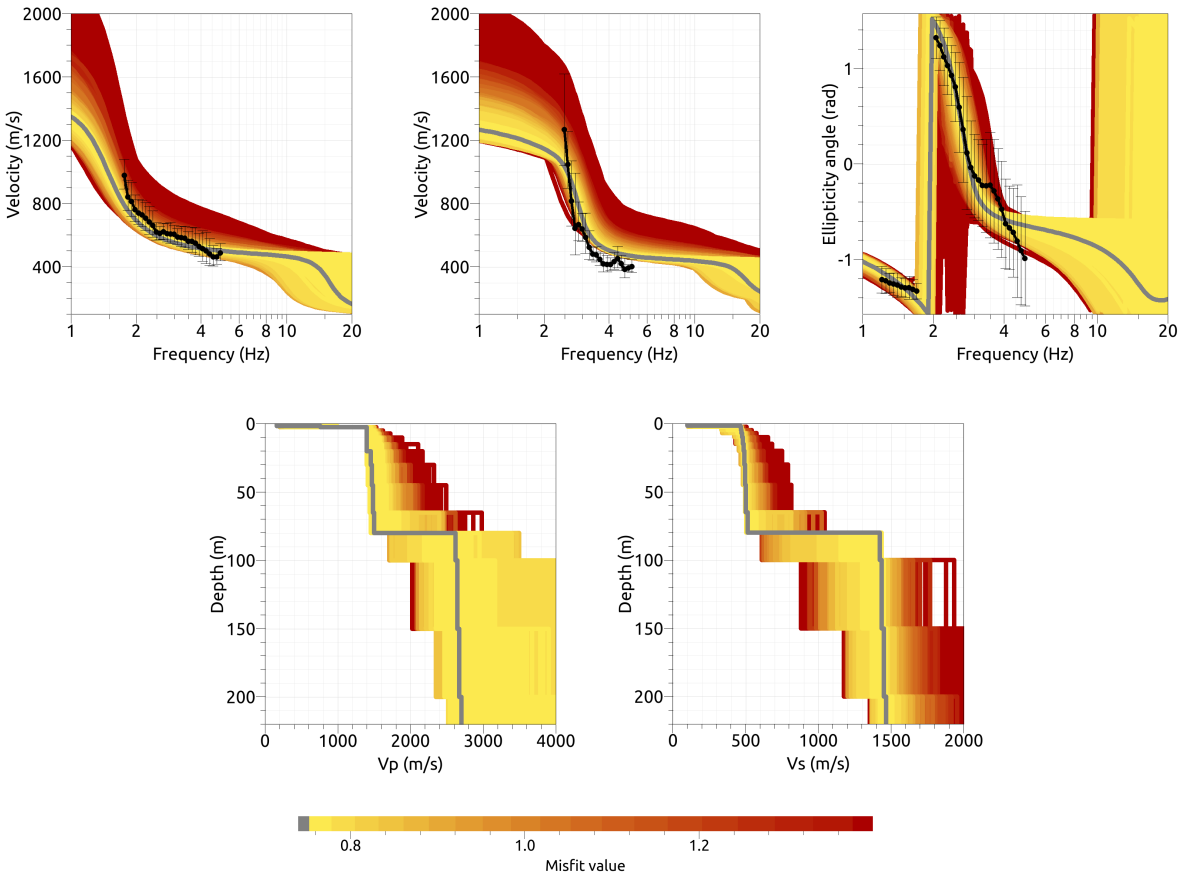

Figure 20: Inversion SDESfix. Top line: Dispersion curves for the Love wave fundamental mode (left) and the Rayleigh wave fundamental mode (center) and ellipticity curves of the Rayleigh wave fundamental mode (right). Bottom line: P-wave velocity profiles (left) and S-wave velocity profiles (right). The black dots indicate the data points used for the inversion, the gray line indicates the best-fitting model.

4.4 Overview of the inversion result

The best-fitting models of the inversions are shown in Fig. 21. The models are very similar. The smallest wavelength contained in the dispersion curves was around 78 m, so that we cannot expect to resolve details in the shallowest layers. In the superficial 1.5 m, we find major differences in the models. The 4-layer and 5-layer inversions find S-wave velocities of around 150 m/s here, while the fixed-layer approach finds a velocity of 100 m/s. The 6-, 7- and 8-layer inversions, however, do not find low velocities at the surface and indicate a velocity of around 470 m/s here. Below 1.5 m, all models are in very good agreement. The S-wave velocity gradually increases from about 460 to 490 m/s to about 480 to 500 m/s at 65 m of depth. A strong velocity contrast is found at 79 to 82 m of depth, where the velocity increases to values between 1400 and 1500 m/s. The V_{S30} value for the inversions ranges from 391.9 to 483.7 m/s (average value 456.5 $\pm$ 35.6 m/s). This corresponds to soil class B in EC8 and C in SIA261.

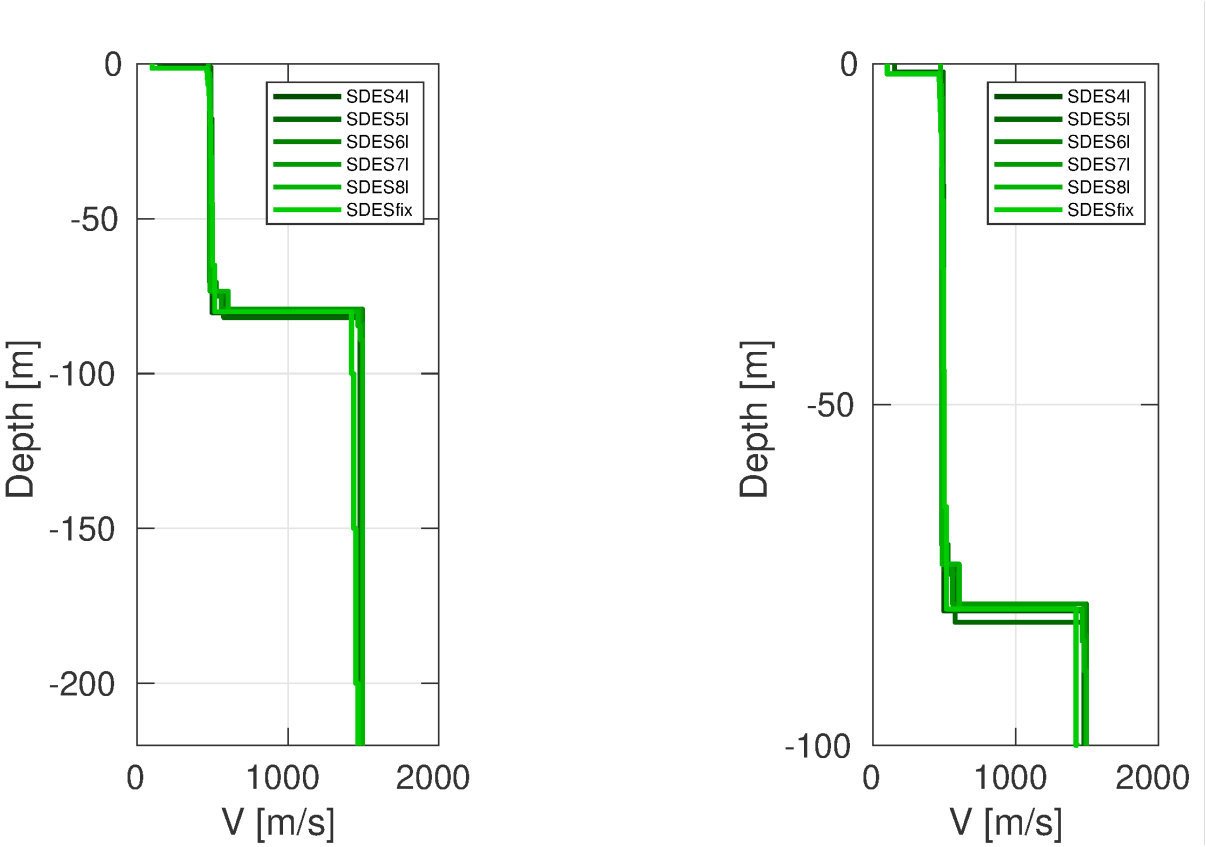

Figure 21: Overview of shear-wave velocity profiles of the best-fitting models of all inversions (left) and a zoom on the shallow part (right).

The dispersion curves measured with array 1 did not match the ones of array 2. If they do not correspond to the fundamental mode, they might still correspond to a harmonic mode of the respective wave type. In order to test this hypothesis, we calculated the theoretical dispersion curves for the first five modes of Love and Rayleigh waves for the best-fitting models of the respective inversions. The results are plotted together with the different measured dispersion curves in Fig. 22. The fundamental mode curves fit well with the measurements, as they were used as inversion targets. The dispersion curves of array 1, however, cannot be explained by higher modes, but the high-frequency part of the dispersion curves might also not be well constrained as no information above 5.11 Hz was used for the inversion. A possible explanation is that array 1 could be mainly located on infill that was done during the construction of the parking space at this area. In any case, we cannot explain the measurements of array 1.

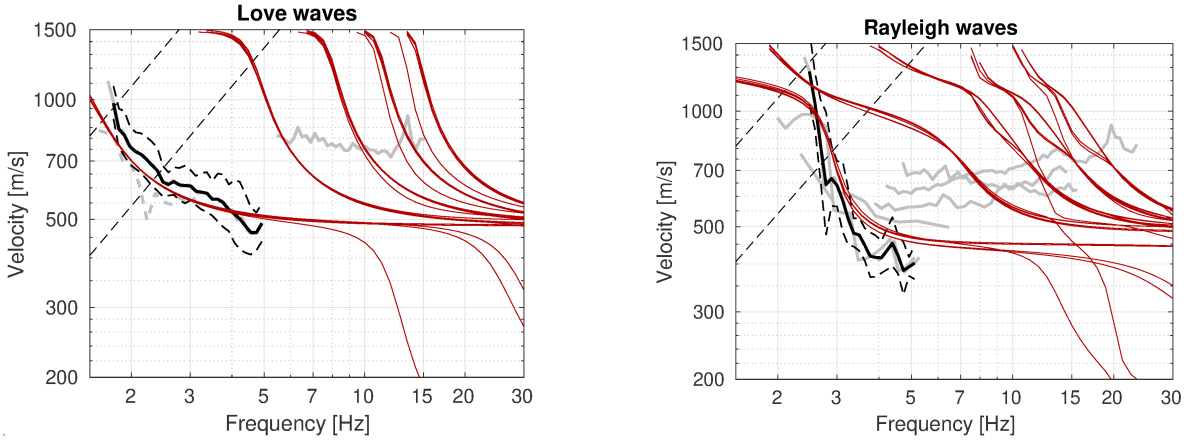

Figure 22: Comparison of the Love (left) and Rayleigh (right) wave dispersion curves measured (in gray), used for the inversion (in black) and resulting from the best models of the inversions (in red). The first five modes for the best models resulting from inversions SDES4l-SDESfix are shown.

4.5 Site amplification

In Fig. 23, the theoretical amplification function for the best models resulting from the inversions is compared with the empirical amplification of station SDES, based on 30 events so far. The empirical amplification shows a first peak at around 1.5 Hz, followed by a trough at about 3 Hz. Afterwards, there is a slight increasing trend with more variability.
The curve for the inversion models actually fits very well to this empirical amplification. The peak frequency is slightly higher (1.6 Hz) and the amplification at the peak is smaller. The trough matches very well. For the higher-frequency part, the modeled amplification shows more peaks and troughs than the empirical amplification of the stations. This might be explained by edge-generated surface waves, which cannot be modeled using the 1-dimensional SH resonance.

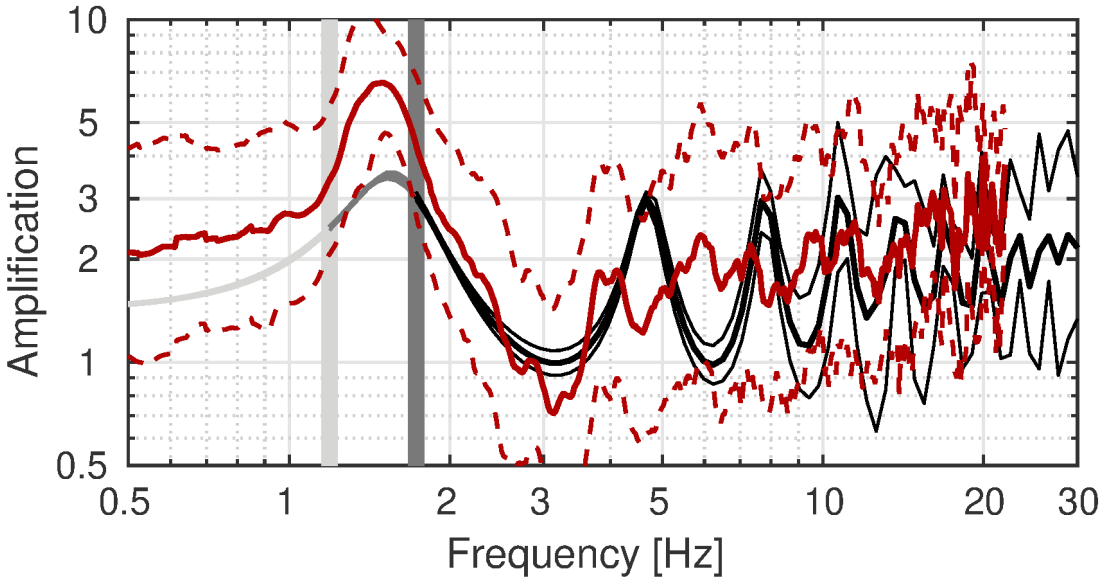

Figure 23: Comparison between the modeled amplification for the final set of best models of the different inversions (SDES4l-SDESfix; in grey to black, with standard deviation) and the empirical amplification measured at station SDES (red, with standard deviation). The vertical light and dark grey bars correspond to the lowest frequency of the ellipticity and dispersion curves, respectively.

4.6 Quarter-wavelength representation

The quarter-wavelength velocity approach (Joyner et al., 1981) provides, for a given frequency, the average velocity at a depth corresponding to 1/4 of the wavelength of interest. It is useful to identify the frequency limits of the experimental data (the minimum frequency of the dispersion curve used in the inversion is 1.76 Hz, the minimum frequency used for the ellipticity inversion 1.20 Hz). The results using this proxy show that the dispersion curves constrain the profiles down to about 68 m, but the ellipticity information down to more than 150 m (Fig. 24). Moreover, the quarter wavelength impedance-contrast introduced by Poggi et al. (2012) is also displayed in the figure. It corresponds to the ratio between two quarter-wavelength average velocities, respectively from the top and the bottom part of the velocity profile, at a given frequency (Poggi et al., 2012). This curve shows a strong contrast at the fundamental frequency of the site.

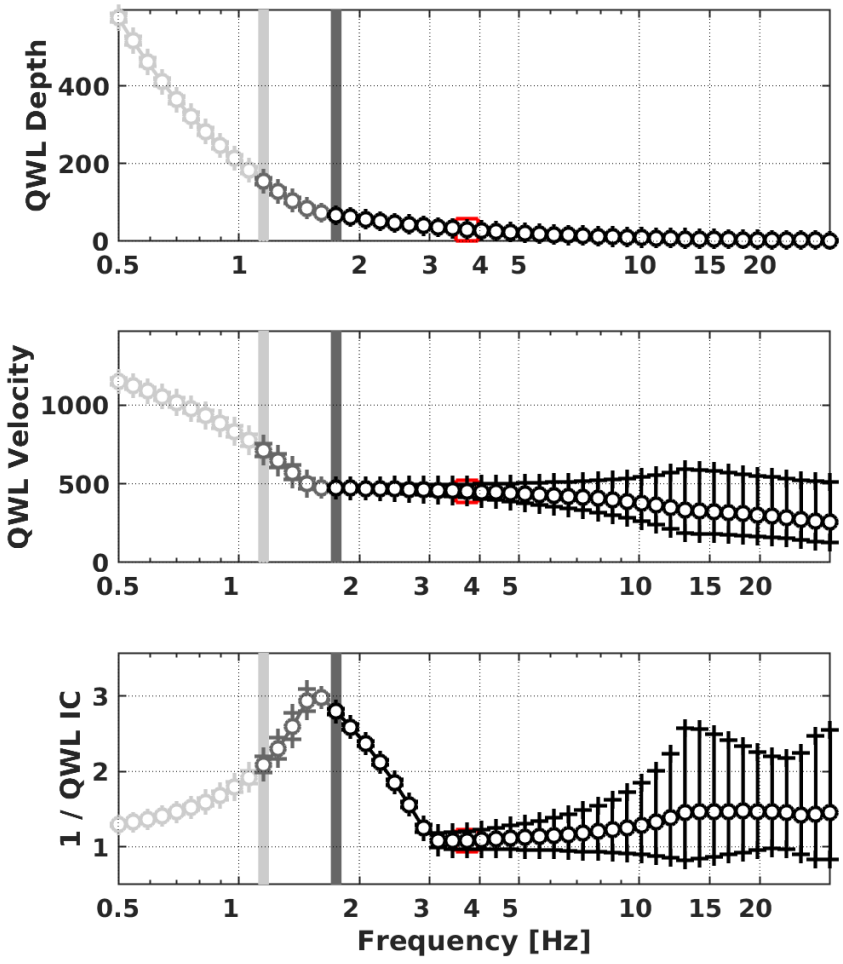

Figure 24: Quarter wavelength representation of the velocity profile for the best models of the inversions (top: depth, center: velocity, bottom: inverse of the impedance contrast). The black curves are constrained by the dispersion curves, the light grey curves are not constrained by the data. The red square corresponds to V_{S30}.

5 Conclusion

We performed a passive array measurement with two arrays to characterize the soil underneath station SDES in Delémont (JU), located on fine-graines scree deposits.
The dispersion curves for Love and Rayleigh waves measured at both arrays do not fit, therefore the results of the smaller array measurement were not used further. For the larger array, the dispersion curves were measured from 1.76 to 4.92 Hz for Love waves and from 2.48 to 5.11 Hz for Rayleigh waves. The ellipticity peak frequency was measured at around 1.79 Hz, corrsponding to a singularity.
The joint inversion of the Love wave dispersion curve with the Rayleigh wave dispersion and ellipticity curves showed that the structure can be explained by models with S-wave velocities of around 480 m/s down to about 65 m of depth, where the velocity increases to over 1400 m/s. At the surface, there might be a layer with low velocities of around 150 m/s with a thickness of less than 1.5 m. The V_{S30} of the best models is about 457 m/s, corresponding to soil class B in EC8 and C in SIA261.

Acknowledgements

The authors thank David Farsky, Dario Chieppa and Dylan Longridge for their help during the array measurements.

References

Aki, K. (1957). Space and time spectra of stationary stochastic waves, with special reference to microtremors. *Bull. Earthquake Res. Inst. Tokyo Univ.*, 35:415–456.

Bettig, B., Bard, P.-Y., Scherbaum, F., Riepl, J., Cotton, F., Cornou, C., and Hatzfeld, D. (2001). Analysis of dense array noise measurements using the modified spatial auto-correlation method (SPAC): application to the Grenoble area. *Boll. Geof. Teor. Appl.*, 42:281–304.

Burjánek, J., Gassner-Stamm, G., Poggi, V., Moore, J. R., and Fäh, D. (2010). Ambient vibration analysis of an unstable mountain slope. *Geophys. J. Int.*, 180:820–828.

Burjánek, J., Moore, J. R., Molina, F. X. Y., and Fäh, D. (2012). Instrumental evidence of normal mode rock slope vibration. *Geophys. J. Int.*, 188:559–569.

Fäh, D., Wathelet, M., Kristekova, M., Havenith, H., Endrun, B., Stamm, G., Poggi, V., Burjanek, J., and Cornou, C. (2009). Using ellipticity information for site characterisation. NERIES deliverable JRA4 D4, available at http://www.neries-eu.org.

Hobiger, M., Bard, P.-Y., Cornou, C., and Le Bihan, N. (2009). Single station determination of Rayleigh wave ellipticity by using the random decrement technique (RayDec). *Geophys. Res. Lett.*, 36.

Joyner, W. B., Warrick, R. E., and Fumal, T. E. (1981). The effect of Quaternary alluvium on strong ground motion in the Coyote Lake, California, earthquake of 1979. *Bull. Seismol. Soc. Am.*, 71(4):1333–1349.

Maranò, S., Reller, C., Loeliger, H.-A., and Fäh, D. (2012). Seismic waves estimation and wavefield decomposition: Application to ambient vibrations. *Geophys. J. Int.*, 191:175–188.

Poggi, V., Edwards, B., and Fäh, D. (2012). Characterizing the Vertical-to-Horizontal ratio of ground motion at soft-sediment sites. *Bull. Seismol. Soc. Am.*, 102(6):2741–2756.

Poggi, V. and Fäh, D. (2010). Estimating Rayleigh wave particle motion from three-component array analysis of ambient vibrations. *Geophys. J. Int.*, 180:251–267.